

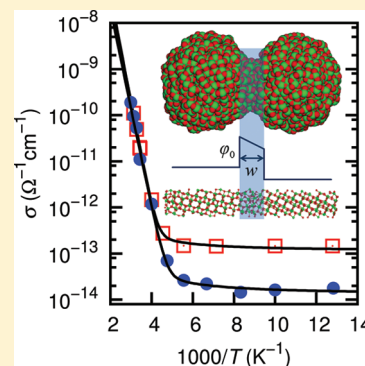
Fluctuation-Induced Tunneling Conductivity in Nanoporous TiO₂ Thin Films

Steven J. Konezny,* Christiaan Richter, Robert C. Snoeberger, III, Alexander R. Parent, Gary W. Brudvig,* Charles A. Schmuttenmaer,* and Victor S. Batista*

Department of Chemistry, Yale University, P.O. Box 208107, New Haven, Connecticut 06520-8107, United States

ABSTRACT: The electronic mechanisms responsible for dark conductivity in nanoporous TiO₂ thin films remain only partially understood, although they control the efficiency of charge transport in a wide range of technological applications. Measurements in the 78–335 K temperature range show DC conductivity values spanning over 4 orders of magnitude, with a high-temperature Arrhenius dependence that gradually changes into a temperature-independent plateau at low temperatures. We show evidence that a fluctuation-induced tunneling conductivity (FITC) mechanism is fully consistent with the experimental data. Quantitative agreement is demonstrated for the entire temperature range ($T = 78–335$ K) with a FITC model parametrized according to atomistic models of nanoporous TiO₂ and the characterization of the films by X-ray diffraction and scanning electron microscopy measurements. These findings suggest that dark DC conductivity in nanoporous TiO₂ films depends strongly on the properties of the junctions linking the constituent nanoparticles.

SECTION: Electron Transport, Optical and Electronic Devices, Hard Matter



Nanoporous TiO₂ thin films have attracted considerable attention due to their pivotal role in energy conversion and environmental applications, including photovoltaics,^{1–3} photocatalysis and remediation of hazardous waste,^{2–5} electrochromic windows and displays,^{3,6,7} and chemical sensors.^{3,8} However, the underlying mechanisms responsible for electron transport through nanoporous TiO₂ remain only partially understood even though they often determine a limiting factor in device performance. Here, we address the mechanism responsible for dark DC conductivity in TiO₂ thin films under vacuum conditions. We find that a fluctuation-induced tunneling conductivity (FITC) mechanism is supported by experimental data for a wide temperature range.

In recent years, there have been significant contributions toward understanding charge transport in nanoporous titania thin films.^{9–19} The most popular models include variable-range hopping (VRH) and/or multiple trap and release (MTR) of electrons in an electrically homogeneous medium containing a distribution of traps. These models have been particularly successful when applied to the conductivity of photogenerated electrons at temperatures experimentally accessible in a native device environment. However, they predict a temperature (T) dependence of the dark DC conductivity of the form $\ln \sigma \propto T^{-\alpha}$, where $\alpha = 1$ in the MTR model²⁰ and $\alpha = 1/4$ for VRH.²¹ As shown in Figure 1, such a dependence does not account for the observed saturation of dark conductivity at low temperature, as reported here and elsewhere.^{22–25} In contrast, the FITC model offers a proper description of conductivity over the entire temperature range with a single set of structural parameters, predicting not only the Arrhenius high-temperature behavior but also the temperature-independent tunneling regime at low temperature.

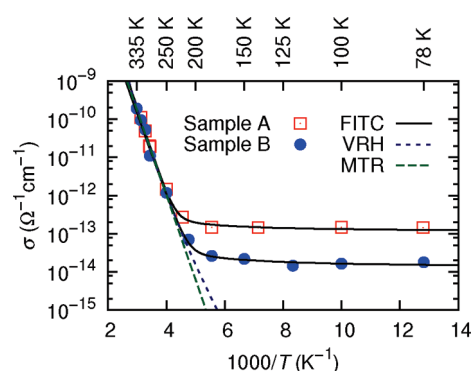


Figure 1. Arrhenius plot of the dark DC conductivities of nanoporous TiO₂ films, made by sintering Sigma–Aldrich (sample A; filled circles) and Ishihara (sample B; open squares) nanoparticles. The solid lines are obtained using the fluctuation-induced tunneling conduction (FITC) model. The short-dashed and long-dashed lines are the results when using the variable-range hopping (VRH) and multiple trap and release (MTR) models, respectively. Temperatures in K are shown on the top axis for convenience.

Because the model can be closely tied to the nanoporous film microstructure, it should provide valuable insight for the development of high-performance electrode materials.

FITC models have been extensively applied to a variety of systems with heterogeneous microstructures, including carbon

Received: June 23, 2011

Accepted: July 14, 2011

Published: July 14, 2011

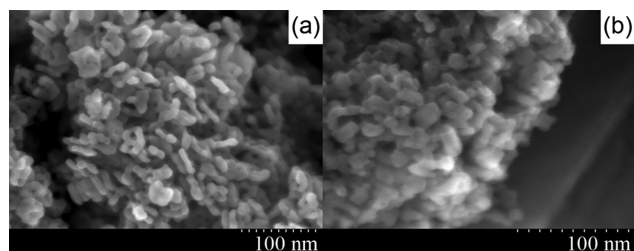


Figure 2. SEM images of sintered TiO₂ nanoparticle films made from (a) Sigma–Aldrich and (b) Ishihara ST-01 nanoparticles.

polyvinylchloride films,^{26,27} polycarbonate composite films containing microcrystalline charge-transfer complexes,²⁸ tin-doped indium oxide nanoparticle films,²⁹ microcrystalline silicon,^{30,31} and carbon nanotube bundles.³² Here, we propose FITC to model the dark DC conductivity of TiO₂ thin films prepared by sintering nanoparticles as found in solar cells or environmental applications. The model predicts temperature-independent conductivity at low temperatures, reflecting simple inelastic tunneling, and a gradual transition to exponential Arrhenius-type (linear in $\ln \sigma$ versus $1/T$) behavior at high temperature, as observed in experiments (see Figure 1).

For typical TiO₂ thin-film dimensions and preparation conditions, the asymptotic low-temperature conductivity is very small ($\sigma \approx 10^{-13} \Omega^{-1} \text{cm}^{-1}$) and therefore difficult to measure. In fact, most conductivity measurements reported to date have been limited to the high-temperature regime where the Arrhenius-type behavior predicted by the FITC model is indistinguishable from models based solely on thermally activated processes. It is therefore not surprising that the FITC mechanism has been largely overlooked. In this Letter, we address dark DC conductivities over a wide temperature range ($T = 78\text{--}335 \text{ K}$). In addition to the high sensitivity measurements of electrical conductivity, we characterize the samples by scanning electron microscope (SEM) images (see Figure 2), powder X-ray diffraction (XRD) measurements, and atomistic modeling to provide insight into the microstructure and electrically heterogeneous nature of the TiO₂ thin films closely tied to the FITC mechanism. These structural data are essential to build a charge-transport model that takes into account the barriers for electron transport through the nanoparticle contact junctions.³³

Fluctuation-Induced Tunneling Conduction Model. Building upon FITC models previously applied to describe conductivity in other systems of comparable microstructure,^{27,28,31} we model the TiO₂ thin films as networks of contact junctions where noncrystalline TiO₂ regions connect the crystalline anatase centers of TiO₂ nanoparticles (see the SEM images in Figure 2 and the representations depicted in Figure 3). The tunneling rate across a junction depends on the effective area A at the region of closest approach between crystallites, the effective tunneling width w of the noncrystalline region of the junction, and the zero-field barrier height ϕ_0 , which is primarily the result of the conduction band offset between the crystalline and noncrystalline TiO₂ phases.

With typical junction parameters (e.g., $A \approx 50 \text{ nm}^2$, $w \approx 3\text{--}4 \text{ nm}$; see Table 1) and a static dielectric constant of $\epsilon_r \approx 40$ inside of the junction,³⁴ the effective junction capacitance $C = \epsilon_r \epsilon_0 A/w$ is very small (on the order of 10^{-6} pF). Therefore, thermal fluctuations in the density of the free electrons near the junction generate strong voltage fluctuations V_T with $\langle V_T^2 \rangle =$

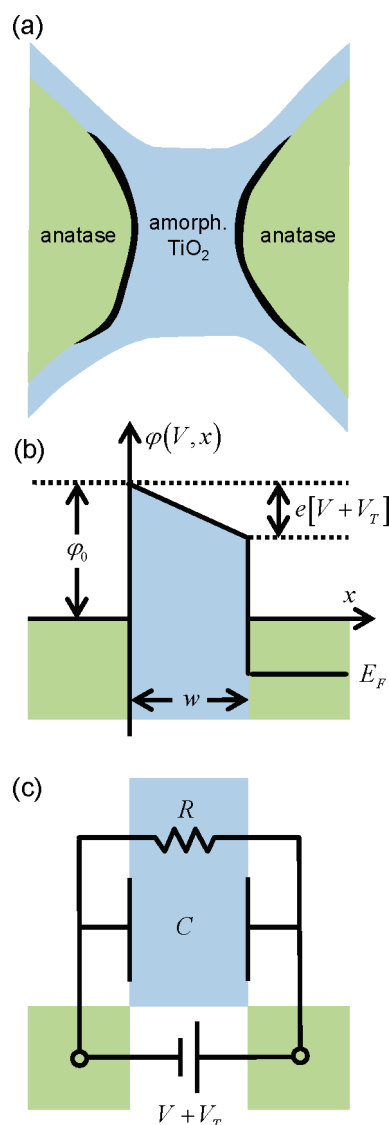


Figure 3. (a) Tunnel junction composed of a noncrystalline TiO₂ region (blue) between two TiO₂ nanocrystallites (green) that forms at the nanoparticle connection, with heavy lines indicating the area where most of the tunneling occurs. (b) Energy diagram showing the barrier potential under a bias of $V + V_T$, where V is the voltage across the junction due to the applied voltage and V_T is the voltage fluctuation due to thermally generated charge density fluctuations in the crystalline regions. (c) Equivalent RC circuit of the junction.

$k_B T/C$, where k_B is the Boltzmann constant. Upon averaging, these fluctuations can increase the tunneling probability by effectively reducing the width and height of the barrier due to the superposition of the applied and thermally generated electric fields (see Figure 3). Note that the resulting Boltzmann distribution $P(\mathcal{E}) = (a/\pi k_B T)^{1/2} \exp(\mathcal{E}^2/k_B T)$ of thermally generated electric field fluctuations $\mathcal{E}_T = V_T/w$ has a width related to the charging energy $E_c = CV_T^2/2 = a\mathcal{E}_T^2$ required to displace the capacitor from equilibrium, where $a = \epsilon_r \epsilon_0 Aw/2$.

The resulting fluctuation-induced tunneling conductivity of the TiO₂ thin film is³⁵

$$\sigma(\mathcal{E}) = \frac{\gamma \langle j(\mathcal{E}) \rangle A}{tV} \quad (1)$$

Table 1. Nanocrystallite Diameter d_{nc} Measured by XRD and FITC Model Fitting Parameters Used for Samples A and B in Figure 1^a

	d_{nc} (nm)	φ_0 (meV)	w (nm)	A (nm ²)	d_j (nm)
A	17.0	421	3.45	71.6	9.54
B	15.9	388	3.73	22.5	5.35

^a A , w , and φ_0 are the effective area, width, and zero-field barrier height of the junction, respectively, and d_j is the effective junction diameter given by $d_j \equiv 2(A/\pi)^{1/2}$.

where t is the thickness of the sample, V is the voltage across the junction, γ is the sheet-conductance proportionality constant,³⁰ and $\langle j(\mathcal{E}) \rangle$ is the thermal average of the net current density $j(\mathcal{E})$ in the direction of the applied field³¹

$$j(\mathcal{E}) = \frac{mqk_B^2 T^2}{2\pi^2 \hbar^3} \left(\left\{ \frac{e^{-2\chi w \xi}}{T'} (1 - e^{-T' q \mathcal{E} w / k_B T}) \right\} + \left\{ \frac{e^{-2\chi w \xi}}{1 + T'} (1 - e^{-T' q \mathcal{E} w / k_B T}) \right\} + \{ e^{-\varphi_m / k_B T} (1 - e^{-q \mathcal{E} w / k_B T}) \} + \left\{ \frac{e^{-2\chi w \xi}}{1 - T'} [(1 - e^{-(1 - T') \varphi_m / k_B T}) - (1 - e^{-(1 - T')(\varphi_m + q \mathcal{E} w) / k_B T}) e^{-T' q \mathcal{E} w / k_B T}] \right\} \right) \quad (2)$$

where \hbar is the reduced Planck constant, m is the charge carrier mass, q is the electron charge, $\chi = (2m\varphi_0/\hbar^2)^{1/2}$ is the tunneling constant, the dimensionless temperature-dependent parameter is given by $T' = 2\chi w \eta k_B T / \varphi_0$, and φ_m is the maximum in the field-corrected barrier. The dimensionless parameters ξ and η are field dependent and originate from the first two terms in a power series expansion of the exponent of the transmission coefficient under the WKB approximation.³⁶

Both the Arrhenius and temperature-independent regimes in the observed fluctuation-induced tunneling conductivity are described by eq 2. Each of the four terms in curly brackets includes a forward current density component in the direction of the applied electric field and a backflow current density in the opposite direction. The first term is the net current density in the low-temperature limit, with an abrupt change in the density of states at the Fermi energy, while the other terms are corrections obtained by expanding the Fermi–Dirac distribution to first order in temperature. The second term corresponds to the correction to the density of occupied states below the Fermi energy. The third term is the net current density due to electrons in the exponential tail of the distribution above the Fermi energy that are higher in energy than φ_m and are assumed to have a transmission coefficient equal to 1 (i.e., thermal activation over the barrier). The last term in curly brackets is the net current density of electrons at energies above the Fermi energy with a transmission coefficient less than 1 (i.e., thermally activated tunneling).

Experimental Methods. Anatase nanoparticles were obtained from Sigma–Aldrich Corporation and Ishihara Corporation with diameters of <25 and 7 nm, respectively. TiO₂ (1.5 g) was added to 1.3 mL of water, followed by sonication for 15 min. For the conductivity measurements, the nanoparticle slurry was

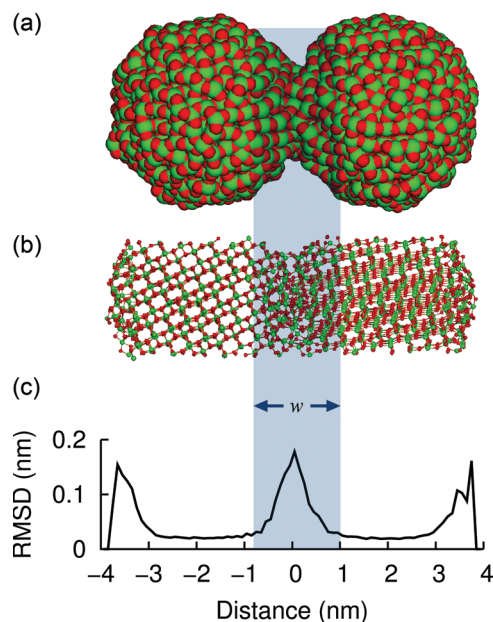


Figure 4. (a) Molecular dynamics simulation results of two 4 nm particles sintered at 450 °C. (b) Cylindrical sample cut from (a) showing the crystalline anatase core and noncrystalline shell of the nanoparticles. (c) Average atomic rmsd relative to bulk anatase.

spread onto a bottom electrode between two fiberglass spacers, which were $200 \pm 4 \mu\text{m}$ thick with a measured resistance $> 200 \text{ T}\Omega$. Immediately thereafter, the top electrode was applied, the excess slurry was removed, and the sample was dried for 24 h at $\sim 70 \text{ }^\circ\text{C}$. Dried samples were annealed at 450 °C for 1 h, the typical sintering conditions used for DSSCs. The sample electrodes were high-chromium-content stainless steel (grade 309). Samples for electrical measurements were lightly clamped with grade 309 bolts to maintain constant sample-to-electrode contact during the measurement and eliminate the effects of thermal expansion. The samples were loaded in a cryostat (Janis ST-100) and kept in the dark under vacuum ($< 20 \text{ mTorr}$) for more than 24 h prior to measurements. A Stanford Research Systems SR570 low-noise current preamplifier was used to supply a 4 V bias and measure the current. To quantify the contact resistance in our devices, we varied the thickness of the TiO₂ nanoparticle films. We found that the use of chromium-rich stainless steel as the contact surface minimizes both the oxide layer formed on the electrode during sintering and the corresponding contact resistance, which is negligible compared to the resistance of the TiO₂ film. The films for the XRD (Bruker D8 with Cu K α radiation) and SEM characterization were prepared by doctor blading the TiO₂/water slurry on glass and FTO/glass substrates, respectively. The nanocrystallite diameters reported in Table 1 were determined by applying Scherrer's semiempirical formula to the (101) Bragg peak.

Atomistic Structure Modeling. An atomistic model of the contact junctions connecting TiO₂ nanoparticles was obtained by sintering anatase nanoparticles using annealing molecular dynamics simulations, after thermalization of the system at 450 °C. Simulations were performed by using the LAMMPS package³⁷ in the NVT ensemble with the temperature maintained at 450 °C using a Nosé–Hoover thermostat with a damping time of 10 fs. The atomic positions and velocities were updated using the velocity-Verlet algorithm with a time step of

1 fs and a total runtime of 250 ps. The force field by Matsui and Akaogi³⁸ was used to describe the interactions between the atoms of the nanoparticles, as in previous work.³⁹ To obtain the atomic root-mean-squared deviation (rmsd) in the noncrystalline regions of sintered nanoparticles, the anatase crystal structure was aligned to the crystalline core of each nanoparticle, and the rmsd data were averaged over the final 100 ps of the molecular dynamics trajectory. Particles >4 nm in diameter were chosen for the multiphase structural modeling to be representative of larger nanoparticles.

Electron-Transport Mechanism in Nanoporous TiO₂. Figure 1 shows the temperature-dependent dark DC conductivity of nanoporous TiO₂ thin films made from Sigma–Aldrich and Ishihara ST-01 nanoparticles and the corresponding conductivity curves determined by the FITC model, with structural parameters given in Table 1. Two characteristic regimes of FITC are clearly visible in this extended temperature range, the thermally activated high-temperature regime ($T > 250$ K) and the temperature-independent regime ($T < 150$ K). Figure 1 also shows the limitations of VRH and MTR models.⁴⁰ Note that the FITC model agrees with the dark DC conductivity data over the entire temperature range, including both the high- and low-temperature regimes, while the VRH and MTR models can only account for one of these regimes with a unique set of parameters.

The effective zero-field barrier heights of 0.42 and 0.39 eV extracted from the conductivity measurements using the FITC model for samples A and B, respectively, are comparable to the activation energies E_a measured for the high-temperature data in this and other works^{22–25} because the slope of $\ln \sigma$ versus $1/T$ in this temperature regime is largely determined by ϕ_0 ($\phi_0 \approx E_a$). Under the MTR model, E_a is related to the distribution of trap states below the conduction band, which have been attributed to oxygen vacancies, Ti³⁺ states, and interface states.^{22–25,41} E_a is therefore dependent on measurement and fabrication conditions such as the ambient oxygen pressure and N-doping.^{23–25,41} In the FITC model, ϕ_0 is due to the conduction band offset at the junction and can also be affected by defect states because they can reduce the effective barrier height for tunneling, though it is the defect states at the contact junction that are relevant. It is worth noting that the low-temperature plateau in the conductivity of sample A is nearly an order of magnitude lower than that of sample B, reflecting both a larger barrier height and a wider tunneling width (see Table 1). Increasing ϕ_0 tends to decrease the low-temperature plateau conductivity in addition to increasing the slope of $\ln \sigma$ versus $1/T$ in the high-temperature region, while increasing the tunneling width w only reduces the former.³⁰ In the range of tunnel junction parameters studied, increasing the effective junction area A increases the conductivity for the entire temperature range studied with negligible effect on the high-temperature slope. Therefore, learning how to optimize A and control ϕ_0 , for example, by determining materials that generate lower conduction band offsets or fabrication conditions that optimize the defect distributions at the contact junctions, is of particular interest for technological applications because the conductivity is most sensitive to these parameters at room temperature.

Contact Junction Characterization. Figure 4a shows a representative configuration of two sintered TiO₂ nanoparticles, as obtained by annealing molecular dynamics simulations at 450 °C. A cylindrical sample extracted from these two nanoparticles, shown in Figure 4b, reveals the internal atomic structure with noncrystalline TiO₂ at the contact junction and nanoparticle

surface. The analysis of atomic rmsds relative to the anatase crystal structure shown in Figure 4c quantifies the disorder observed in the noncrystalline phase at the junction and extremities of the cylindrical core. These rmsds clearly indicate that the TiO₂ nanoparticles have a noncrystalline shell surrounding the crystalline core. This core–shell structure is consistent with reports of the overall TiO₂ nanoparticle size, obtained from microscopy data, being larger than the nanocrystallite size, determined by XRD.⁴² For example, the average particle sizes seen by SEM (see Figure 2) are larger than the nanocrystallite diameter determined from XRD (see Table 1). These results also agree with conductivity measurements of unsintered, spin-coated nanoparticle thin films that display both thermally activated and temperature-independent conductivity regimes,²² suggesting fluctuation-induced carrier tunneling between crystalline cores through noncrystalline shells.

Our molecular dynamics simulations and SEM and XRD data show that tunneling junctions are formed when sintering nanoporous TiO₂ due to its multiphase composition. The junction dimensions are determined by the widths of the noncrystalline regions and the areas of closest approach between nanocrystallites. It follows that the barrier heights of the tunneling junctions are due to the energy difference between the conduction band of crystalline anatase and the mobility edge of noncrystalline TiO₂ (see Figure 3). This picture is consistent with the values of ϕ_0 for samples A and B extracted from the conductivity measurements using the FITC model. Furthermore, the FITC model is consistent with optical pump/THz probe measurements, providing evidence that, even though the DC conductivity of photoexcited nanocrystalline TiO₂ and ZnO is suppressed relative to bulk values, the AC conductivity is within a factor of 2–4 of the single-crystal DC value.^{11,43} These data indicate that the carriers are relatively mobile within a given particle, but their net conductivity is limited by interparticle transport. We note, however, that our observations are limited to vacuum conditions, while the presence of impurities, gas, or an electrolyte at the junctions is expected to have an impact on the shape of the barriers and therefore on the overall conductivity through the nanoparticle network. These effects, of course, have great technological significance and will be the focus of future work. Nevertheless, none of these additional factors are expected to change the underlying transport mechanism through energy barriers at contact junctions.

CONCLUSIONS

We demonstrated that electron transport in nanoporous TiO₂ thin films can be accurately described by a FITC model. The model is in quantitative agreement with dark DC conductivity measurements over an extended temperature range ($T = 78–335$ K). The structural parameters extracted from the conductivity data, using the FITC model, are consistent with the characterization of sintered TiO₂ nanoparticle films by SEM, XRD, and annealing molecular dynamics simulations of sintered TiO₂ nanoparticles. These data reveal the formation of noncrystalline regions between the crystalline nanoparticle cores, consistent with energy barriers at the junctions. These findings suggest that improvements in electron transport in emerging technologies based on nanoporous TiO₂ electrodes could be achieved by focusing on ways to optimize the TiO₂ nanoparticle interconnectivity and studying the impact of sintering conditions, particle size and shape, choice of electrolyte, ambient

oxygen and water content, doping, and other fabrication conditions on the dimensions and alignment of electronic energy levels at the interparticle contact junctions.

AUTHOR INFORMATION

Corresponding Author

*E-mail: steven.konezny@yale.edu (S.J.K.); gary.brudvig@yale.edu (G.W.B.); charles.schmuttenmaer@yale.edu (C.A.S.); victor.batista@yale.edu (V.S.B.).

ACKNOWLEDGMENT

The authors acknowledge support from the Chemical Sciences, Geosciences, and Biosciences Division, Office of Basic Energy Sciences, Office of Science, U.S. DOE (Grant DE-FG02-07ER15909). The NSF Graduate Research Fellowship to A.R.P. and Grants ECCS-0404191 and CHE 0911520 funded the development of methods for preparation of computational structural models of TiO₂.

REFERENCES

- (1) Barbe, C. J.; Arendse, F.; Comte, P.; Jirousek, M.; Lenzmann, F.; Shklover, V.; Grätzel, M. Nanocrystalline Titanium Oxide Electrodes for Photovoltaic Applications. *J. Am. Ceram. Soc.* **1997**, *80*, 3157–3171.
- (2) Grätzel, M. Mesoscopic Solar Cells for Electricity and Hydrogen Production from Sunlight. *Chem. Lett.* **2005**, *34*, 8–13.
- (3) Chen, X.; Mao, S. S. Titanium Dioxide Nanomaterials: Synthesis, Properties, Modifications, and Applications. *Chem. Rev.* **2007**, *107*, 2891–2959.
- (4) Hoffmann, M.; Martin, S.; Choi, W.; Bahnemann, D. Environmental Applications of Semiconductor Photocatalysis. *Chem. Rev.* **1995**, *95*, 69–96.
- (5) Carp, O.; Huisman, C. L.; Reller, A. Photoinduced Reactivity of Titanium Dioxide. *Prog. Solid State Chem.* **2004**, *32*, 33–177.
- (6) Bechinger, C.; Ferrere, S.; Zaban, A.; Sprague, J.; Gregg, B. A. Photoelectrochromic Windows and Displays. *Nature* **1996**, *383*, 608–610.
- (7) Granqvist, C. G. Transparent Conductors as Solar Energy Materials: A Panoramic Review. *Sol. Energy Mater. Sol. Cells* **2007**, *91*, 1529–1598.
- (8) Tiemann, M. Porous Metal Oxides as Gas Sensors. *Chem.—Eur. J.* **2007**, *13*, 8376–8388.
- (9) de Jongh, P. E.; Vanmaekelbergh, D. Trap-Limited Electronic Transport in Assemblies of Nanometer-Size TiO₂ Particles. *Phys. Rev. Lett.* **1996**, *77*, 3427–3430.
- (10) Dittrich, T.; Weidmann, J.; Koch, F.; Uhlendorf, I.; Lauermann, I. Temperature- and Oxygen Partial Pressure-Dependent Electrical Conductivity in Nanoporous Rutile and Anatase. *Appl. Phys. Lett.* **1999**, *75*, 3980–3982.
- (11) Turner, G. M.; Beard, M. C.; Schmuttenmaer, C. A. Carrier Localization and Cooling in Dye-Sensitized Nanocrystalline Titanium Dioxide. *J. Phys. Chem. B* **2002**, *106*, 11716–11719.
- (12) Park, C. O.; Akbar, S. A. Ceramics for Chemical Sensing. *J. Mater. Sci.* **2003**, *38*, 4611–4637.
- (13) Frank, A. J.; Kopidakis, N.; van de Lagemaat, J. Electrons in Nanostructured TiO₂ Solar Cells: Transport, Recombination and Photovoltaic Properties. *Coord. Chem. Rev.* **2004**, *248*, 1165–1179.
- (14) Nelson, J.; Chandler, R. E. Random Walk Models of Charge Transfer and Transport in Dye Sensitized Systems. *Coord. Chem. Rev.* **2004**, *248*, 1181–1194.
- (15) Boschloo, G.; Hagfeldt, A. Activation Energy of Electron Transport in Dye-Sensitized TiO₂ Solar Cells. *J. Phys. Chem. B* **2005**, *109*, 12093–12098.
- (16) Peter, L. M.; Walker, A. B.; Boschloo, G.; Hagfeldt, A. Interpretation of Apparent Activation Energies for Electron Transport in Dye-Sensitized Nanocrystalline Solar Cells. *J. Phys. Chem. B* **2006**, *110*, 13694–13699.
- (17) Kopidakis, N.; Benkstein, K. D.; van de Lagemaat, J.; Frank, A. J.; Yuan, Q.; Schiff, E. A. Temperature Dependence of the Electron Diffusion Coefficient in Electrolyte-Filled TiO₂ Nanoparticle Films: Evidence Against Multiple Trapping in Exponential Conduction-Band Tails. *Phys. Rev. B* **2006**, *73*, 045326.
- (18) Bisquert, J. Hopping Transport of Electrons in Dye-Sensitized Solar Cells. *J. Phys. Chem. C* **2007**, *111*, 17163–17168.
- (19) Jennings, J. R.; Ghicov, A.; Peter, L. M.; Schmuki, P.; Walker, A. B. Dye-Sensitized Solar Cells Based on Oriented TiO₂ Nanotube Arrays: Transport, Trapping, and Transfer of Electrons. *J. Am. Chem. Soc.* **2008**, *130*, 13364–13372.
- (20) Tiedje, T.; Cebulka, J. M.; Morel, D. L.; Abeles, B. Evidence for Exponential Band Tails in Amorphous Silicon Hydride. *Phys. Rev. Lett.* **1981**, *46*, 1425–1428.
- (21) Mott, N. F.; Davis, E. A. *Electronic Properties in Non-Crystalline Materials*; Oxford University Press: New York, 1971.
- (22) Hassan, A. K.; Chaure, N. B.; Ray, A. K.; Nabok, A. V.; Habesch, S. Structural and Electrical Studies on Sol–Gel Derived Spun TiO₂ Thin Films. *J. Phys. D: Appl. Phys.* **2003**, *36*, 1120–1125.
- (23) Barborini, E.; Bongiorno, G.; Forleo, A.; Francioso, L.; Milani, P.; Kholmanov, I.; Piseri, P.; Siciliano, P.; Taurino, A.; Vinati, S. Thermal Annealing Effect on Nanostructured TiO₂ Microsensors by Supersonic Cluster Beam Deposition. *Sens. Actuators, B* **2005**, *111–112*, 22–27.
- (24) Pomoni, K.; Vomvas, A.; Trapalis, C. Dark Conductivity and Transient Photoconductivity of Nanocrystalline Undoped and N-Doped TiO₂ Sol–Gel Thin Films. *Thin Solid Films* **2008**, *516*, 1271–1278.
- (25) Reddy, K. M.; Manorama, S. V.; Reddy, A. R. Bandgap Studies on Anatase Titanium Dioxide Nanoparticles. *Mater. Chem. Phys.* **2003**, *78*, 239–245.
- (26) Sheng, P.; Sichel, E. K.; Gittleman, J. I. Fluctuation-Induced Tunneling Conduction in Carbon-Polyvinylchloride Composites. *Phys. Rev. Lett.* **1978**, *40*, 1197–1200.
- (27) Sheng, P. Fluctuation-Induced Tunneling Conduction in Disordered Materials. *Phys. Rev. B* **1980**, *21*, 2180–2195.
- (28) Paschen, S.; Bussac, M. N.; Zuppiroli, L.; Minder, E.; Hilti, B. Tunnel-Junctions in a Polymer Composite. *J. Appl. Phys.* **1995**, *78*, 3230–3237.
- (29) Ederth, J.; Johnsson, P.; Niklasson, G. A.; Hoel, A.; Hultåker, A.; Heszler, P.; Granqvist, C. G.; van Doorn, A. R.; Jongerius, M. J.; Burgard, D. Electrical and Optical Properties of Thin Films Consisting of Tin-Doped Indium Oxide Nanoparticles. *Phys. Rev. B* **2003**, *68*, 155410.
- (30) Konezny, S. J.; Bussac, M. N.; Geiser, A.; Zuppiroli, L. Charge Transport Mechanisms in Organic and Microcrystalline Silicon Field-Effect Transistors. *Organic Field-Effect Transistors VI*; Society of Photo-Optical Instrumentation Engineers: Bellingham, WA, 2007; p 66580D.
- (31) Konezny, S. J.; Bussac, M. N.; Zuppiroli, L. Charge Transport Mechanisms in Microcrystalline Silicon. *Appl. Phys. Lett.* **2008**, *92*, 012107.
- (32) Salvato, M.; Cirillo, M.; Lucci, M.; Orlanducci, S.; Ottaviani, I.; Terranova, M. L.; Toschi, F. Charge Transport and Tunneling in Single-Walled Carbon Nanotube Bundles. *Phys. Rev. Lett.* **2008**, *101*, 246804.
- (33) There are several studies that consider geometrical narrowing between nanoparticles and its effects on electron trapping in a homogeneous medium,^{13,44,45} though they do not address the inhomogeneous nature of the contact junctions and the barriers to electron transport that they create, as described by the FITC model.
- (34) Ha, H.-K.; Yoshimoto, M.; Koinuma, H.; Moon, B.-K.; Ishiura, H. Open Air Plasma Chemical Vapor Deposition of Highly Dielectric Amorphous TiO₂ Films. *Appl. Phys. Lett.* **1996**, *68*, 2965–2967.
- (35) The conductivity as expressed in eqs 1 and 2 is more explicit than the low-field, low-temperature approximation $\sigma \approx \sigma_0 \exp[-T_1/(T_0 + T)]$ frequently used in the literature, where σ_0 , T_0 , and T_1 are temperature-independent parameters. This simplified expression has a limited range of validity and does not give accurate junction parameter values.

(36) Sakurai, J. J. *Quantum Mechanics*; Addison-Wesley: Reading, MA, 1994.

(37) Plimpton, S. Fast Parallel Algorithms for Short-Range Molecular-Dynamics. *J. Comput. Phys.* **1995**, *117*, 1–19.

(38) Matsui, M.; Akaogi, M. Molecular Dynamics Simulation of the Structural and Physical Properties of the Four Polymorphs of TiO₂. *Mol. Simul.* **1991**, *6*, 239–244.

(39) Koparde, V. N.; Cummings, P. T. Molecular Dynamics Simulation of Titanium Dioxide Nanoparticle Sintering. *J. Phys. Chem. B* **2005**, *109*, 24280–24287.

(40) In Figure 1, the high-temperature conductivity for sample B gives an activation energy of 439 meV and a pre-exponential factor of $7.4 \times 10^{-4} \Omega^{-1} \text{cm}^{-1}$ assuming a thermally activated process (MTR model), while the VRH model gives $\sigma = \sigma_0 \exp[-(T_0/T)^{1/4}]$ with $\sigma_0 = 1.3 \times 10^{20} \Omega^{-1} \text{cm}^{-1}$ and $T_0 = 7.4 \times 10^9 \text{K}$.

(41) Nelson, J.; Eppler, A. M.; Ballard, I. M. Photoconductivity and Charge Trapping in Porous Nanocrystalline Titanium Dioxide. *J. Photochem. Photobiol., A* **2002**, *148*, 25–31.

(42) Yin, H. B.; Wada, Y.; Kitamura, T.; Kambe, S.; Murasawa, S.; Mori, H.; Sakata, T.; Yanagida, S. Hydrothermal Synthesis of Nanosized Anatase and Rutile TiO₂ Using Amorphous Phase TiO₂. *J. Mater. Chem.* **2001**, *11*, 1694–1703.

(43) Baxter, J. B.; Schmuttenmaer, C. A. Conductivity of ZnO Nanowires, Nanoparticles, and Thin Films Using Time-Resolved Terahertz Spectroscopy. *J. Phys. Chem. B* **2006**, *110*, 25229–25239.

(44) Cass, M. J.; Qiu, F. L.; Walker, A. B.; Fisher, A. C.; Peter, L. M. Influence of Grain Morphology on Electron Transport in Dye Sensitized Nanocrystalline Solar Cells. *J. Phys. Chem. B* **2003**, *107*, 113–119.

(45) Nakade, S.; Saito, Y.; Kubo, W.; Kitamura, T.; Wada, Y.; Yanagida, S. Influence of TiO₂ Nanoparticle Size on Electron Diffusion and Recombination in Dye-Sensitized TiO₂ Solar Cells. *J. Phys. Chem. B* **2003**, *107*, 8607–8611.